D 8 High Resolution Spectroscopy

G. Meier[1] and M. Monkenbusch[2]
[1]Institute of Complex Systems, ICS-3
[2]Jülich Centre for Neutron Science 1
Forschungszentrum Jülich GmbH

Contents

1 Introduction 2

2 Principles of Neutron Spin-Echo Spectroscopy 4
  2.1 Example for Spin Echo Spectroscopy 9

3 X-Ray Photon Correlation Spectroscopy 11
  3.1 Examples for X-ray Speckle Pattern 14
  3.2 Example for XPCS Dynamics 16

References 21

Lecture Notes of the 43rd IFF Spring School "Scattering Methods for Condensed Matter Research: Towards Novel Applications at Future Sources" (Forschungszentrum Jülich, 2012).

1 Introduction

In this lecture we are concerned with the extensions of the measurement capabilities in neutron and x-ray scattering beyond that what was known in the seventies regarding neutron scattering and in the nineties regarding x-ray scattering. In table 1 a sketch of the time/energy versus scattering vector/correlation length plane is shown. In this diagram the two relevant techniques under study in this presentation are neutron spin echo spectroscopy (NSE) and X-ray photon correlation spectroscopy (XPCS). The former method extends the usually accessible time/energy range of neutron scattering towards much longer times or lower energies, whereas the x-ray correlation spectroscopy extends the usually accessible Q-range of dynamic light scattering toward much higher Q-values. Since both methods are concerned with an extension of what was known before they are therefore named high resolution techniques, although they deserve this allocation for physically different reasons.

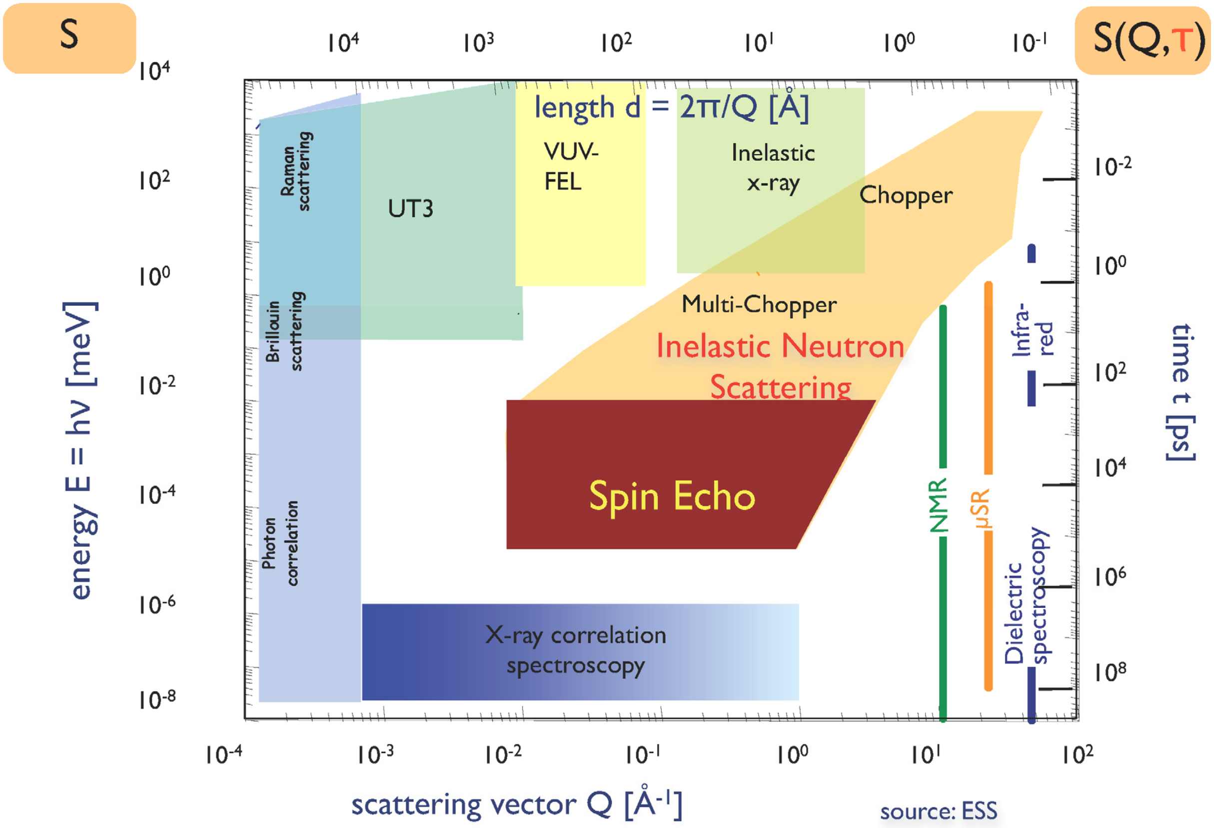

Fig. 1: *Sketch of various spectroscopic techniques with regard to the accessible ranges in the scattering vector Q and correlation time τ.*

X-ray photon correlation spectroscopy, XPCS, similar to dynamic light scattering, DLS, analyses the intensity correlations of scattered electromagnetic radiation. However, the contrast results from physically different properties: index of refraction differences in DLS in contrast to differences in electron density for XPCS. The other mayor difference is the accessible Q-range, mainly due to the used wavelength. The access to very short correlation times is restricted in XPCS, because either the storage ring from the synchrotron has a time structure or the scattering cross section is so small that practically no decent counting statistics can be achieved.

The spin-echo principle stems from the Lamor-precession of polarized neutrons within a magnetic field. In general it is realized via a time of flight spectrometer set-up, in which a time of flight difference for a fixed distance is measured before and after the neutron has interacted with a sample. The probe to do so is the polarisation of the neutrons. According to Fig.1, correlation time values up to several hundreds of nanoseconds are available. Note that the spatial resolution of the scattering experiment is in the nanometer range, which means that a time range of e.g. 100 ns corresponds to effective molecular motion velocities of 1 nm/100 ns = 1 cm/s. This may be compared to the typical neutron velocity of 200-1000 m/s used in these types of experiments. Hence it becomes obvious why NSE is called a high resolution spectroscopic method. The basic idea for this neutron spectroscopy was brought forward by F. Mezei in 1972 [1].

All mentioned scattering techniques aim to measure a scattering function that is closely related to the density-density correlations

$$S_{i,j}\left(\vec{Q},\omega\right)=\frac{1}{2\pi\hbar}\int dt\int d\vec{r}\exp\left(-i\omega t-i\vec{Q}\cdot\vec{r}\left\langle\rho_i\left(\vec{r}'-\vec{r},t\right)\rho_j\left(\vec{r}',t'\right)\right\rangle\right) \tag{1}$$

where $\rho_i(\vec{r},t)$ denotes the density of species i at position $\vec{r}$ and time t. The intermediate scattering function is the Fourier transform of S(Q,ω) in the frequency-time domain:

$$S_{i,j}\left(\vec{Q},t\right)=\hbar\int d\omega\exp\left(i\omega t\right)S_{i,j}\left(\vec{Q},\omega\right) \tag{2}$$

The observed time dependence of S(Q,ω), respectively of the density correlations results from thermal fluctuations (Brownian motions) that are driven by random uncorrelated forces due to coupling to the heat bath.

2 Principles of Neutron Spin-Echo Spectroscopy

The scattering intensity observed in a neutron scattering experiment depends besides trivial factors like the sample amount, transmission and incoming beam intensity on the double differential cross section:

$$\frac{d^2\sigma}{d\Omega dE'} = C\,\frac{k'}{k}\sum_{i,j} b_i b_j\; S_{i,j}(\vec{Q},\omega) \tag{3}$$

where k', k is the modulus of the scattered and incoming neutrons respectively. C is proportional to the amount of sample and b_i is the scattering length of atoms of type i. The energy transfer during scattering is $\hbar\omega = (E - E')$, with E, E' the energies of the incoming and scattered neutrons respectively. The variables of the scattering function depend on $\vec{k}$, $\vec{k}'$; $\vec{Q} = \vec{k} - \vec{k}'$ is the momentum transfer and

$$\hbar\omega = (\hbar^2/2m_n)(k^2 - k'^2) \tag{4}$$

the energy transfer that occurred during the scattering process. $\vec{k}$ relates linearly to $\vec{v}$ (momentum $\vec{p} = m_n\vec{v}$) as to 1/wavelength:

$$\vec{v}m_n = \hbar\vec{k}\,\frac{2\pi}{\lambda} = k \tag{5}$$

It is possible to determine the energy transfer (Eq.4) by measurement of the velocity difference $v' - v$ of the scattered neutrons compared to the incoming neutrons. For large relative velocity changes $\Delta v/v > 1\%$ this measurement could be done by comparing the average velocity of the incoming beam with the velocity distribution of the scattered neutrons. However, if very small differences have to be detected -as it is necessary for the analysis of “soft matter” dynamics- the preparation of a sufficiently narrow velocity distribution of the incoming beam from the continuous (Maxwellian) velocity spectrum emitted by the moderator of the neutron source would leave only a very small and insufficient number of neutrons in the incoming beam.

This situation would immediately improve, if it would be possible to equip each neutron with an individual stop watch which could be read in a way that the run time difference between test tracks before and after the sample is obtained at detection. If this “stop watch” had a sufficient time resolution it would be possible to observe very small velocity changes even if a beam with a wide range of initial neutron velocities is used. This allows to escape the intensity trap.

With some restrictions it is indeed possible to use the neutron spin directions as kind of individual stop watch pointers. The clockwork of this watch is then effected by the precession of the neutron spins in an external magnetic field. The restrictions affecting application are caused by the fact that the “spin-stop watch” can only be read up to an unknown integer number of complete precession turns. Using a polarised incoming beam and a sequence of subsequent spin rotations, the reading is performed by the cosine type transmission function of an analyser and yields only ensemble averages and not individual rotation angles. The intensity at the detector is modulated accordingly. The encountered Δv values are distributed according to $S(Q,\omega \approx k\Delta v)$. The detector signal is then proportional to the integral of precession-angle-cosine modulated intensity contributions with weight according to the distribution of Δv implied by $S(Q,\omega)$. I.e. it is proportional to the cosine-Fourier transform of $S(Q,\omega)$, the intermediate scattering function $S(Q,t)$.

Before we start a more detailed derivation a concrete setup of an NSE spectrometer (see Fig.2) is presented [1,2,3]. A longitudinally polarised neutron beam enters the spectrometer and hits the first so-called $\pi/2$-flipper where the spin is rotated such that on exit it is orthogonal to the longitudinal magnetic field along the following precession path.

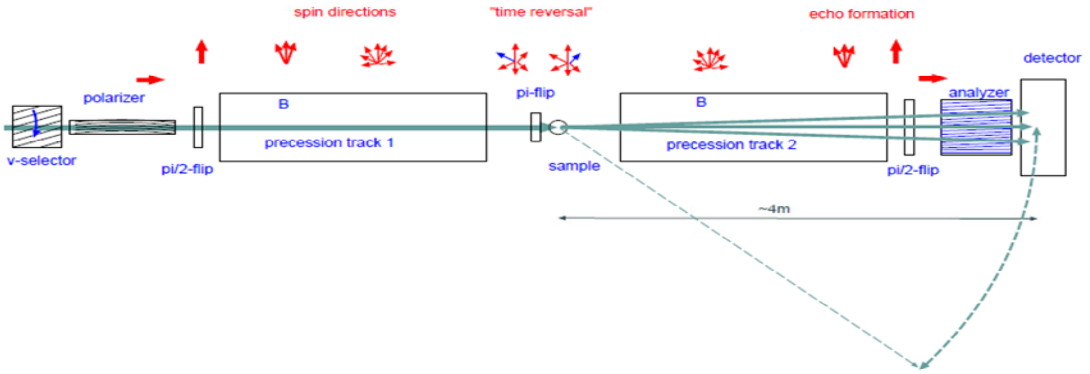

Fig. 2: *The generic setup of a neutron spin-echo spectrometer. Neutrons from a reactor source enter from left, are coarsely monochromatised by a mechanical velocity selector and polarised by reflection from magnetic multilayers. Then with the first π/2- flipper they enter the proper NSE spectrometer and the neutron precession starts. Velocity coding into precession angle is affected by a magnetic field in precession track 1, the π-flipper close to the sample rotates the spin ensemble by 180° and thereby causes an effective "time reversal". Elastic scattering at the sample without velocity change of the neutron then allows the reassembly of all precession angles into a spin-echo. Inelastic scattering at the sample renders this effect less efficient and leads to a reduction of neutron polarisation in the echo condition. This contains the desired information.*

That defines the start of the "spin stop watch", immediately after the flipper a precession of the spins around the axial magnetic field begins. The precession frequency increases during the approach of the center of the main precession solenoid where it reaches its maximum of up to a few MHz. The accumulation of precession angle continues -with decreasing frequency- until the neutrons reach the π-flipper close to the sample (S). The total precession angle at that point is:

$$\Psi = \frac{\gamma}{v}\int_l |B|\,dl = n2\pi + \alpha \tag{6}$$

where $\gamma = 2\pi \times 2913.06598 \times 10^4 \mathrm{s}^{-1}/Tesla$ is the gyromagnetic ratio of the neutrons and $|B|$ is the modulus of the magnetic induction along the path l.

Close to the sample (ideal: at the sample position) the so-called π-flipper is located, it rotates the spins by 180^0 around a vertical axis, thereby the total precession angle is transformed to $\Psi_1 = n2\pi + \alpha \to n2\pi - \alpha$. The parameters n and α are -according to Eq.6 - extremely dependent on velocity and therefore very different for different neutrons in a beam with finite width of the wavelength distribution. As a consequence the spin vectors at the sample position (π-flipper) are evenly distributed on a disc orthogonal to the field direction. If no velocity change occurs during scattering at the sample (elastic scattering) each neutron enters the secondary arm of the spectrometer with unchanged velocity. The precession field and path length of the second arm exactly match the corresponding elements of the primary arm before the sample (π-flipper). Accordingly the precession accumulated in the secondary arm is $\Psi_2 = n2\pi + \alpha$ and the total precession angle at the second $\pi/2$-flippers is $\Psi_1 + \Psi_2 = (n+n)2\pi - \alpha + \alpha = 2n2\pi$. I.e. all spins -irrespective of their initial velocity- reassemble at the same vertical position they had at the start point, the rotation imposed by the second π-flipper converts this back to the initial longitudinal polarisation that is fully restored. The flippers limit the two race tracks and realise “start”, “time reversal” and “stop” of the “spin stop watches”. The second $\pi/2$-flipper is the last element used to manipulate the spins it converts the average precession angle to a longitudinal polarisation component. Since the field after the second $\pi/2$-flipper is again longitudinal, further precessions do not influence the analysed longitudinal polarisation component (the stop watch is stopped!). The analyser consists -like the polariser- of magnetic multilayer mirrors which only reflect neutrons of one longitudinal spin state into the detector. After ensemble averaging this means that the count rate at the detector is proportional to $(1 \pm \cos(\overline{\Psi}))/2$, where $\overline{\Psi}$ is the expectation value of the angle between spin and axial direction.

In the following the relation between detector signal and $S(Q,\omega)$ is derived in terms of mathematical expressions. First the field integrals along the primary and secondary paths of precession are defined:

$$J_1 = \int_{l((\pi/2)_1)}^{l(\pi)} |B|\,dl \tag{7}$$

$$J_2 = \int_{l(\pi)}^{l((\pi/2)_2)} |B|\,dl \tag{8}$$

for a symmetric setup $J_1 = J_2$; $l(\pi,(\pi/2)_{1,2})$ denotes the positions of the corresponding flippers. The precession angle accumulated on a path is

$$\Psi_i = \frac{\gamma J_i}{v} \tag{9}$$

where v is the neutron velocity (typically several 100 m/s). Because the π-flipper inverts the sign of Ψ_1 (i.e. of the part $\Psi_1 \mathrm{m}od\ 2\pi$), a total precession angle of

$$\Psi_{1,2} = -\frac{\gamma J_1}{v} + \frac{\gamma J_2}{v+\Delta v} + 4n\pi \tag{10}$$

results, where Δv is the velocity change of the neutron during scattering and n is an integer. The transmission function of an (ideal) analyser is

$$T_a = \frac{1}{2}[1+\cos(-\frac{\gamma J_1}{v} + \frac{\gamma J_2}{v+\Delta v})] \tag{11}$$

From that the detector intensity

$$I = \eta S(Q)\iint \frac{1}{2}[1 \pm \cos(-\frac{\gamma J_1}{v} + \frac{\gamma J_2}{v+\Delta v})]w_\omega(\Delta v)w_\lambda(v)\, d\Delta v\, dv \tag{12}$$

results, where η is an irrelevant calibration factor and w_ω respectively. w_λ are normalized distribution functions. w_ω represents the spectrum of the sample as found in the scattering function and w_λ takes account for the fact that the NSE spectrometers usually are operated with a broad incoming wavelength distribution ($\Delta\lambda_{FWHM}/\lambda = 10\cdots 20\%$). Observing the linear dependencies of k, $1/\lambda$ and v and series expansion of the squares in Eq.4 and insertion into Eq.12 leads to:

$$I = \eta\iint \frac{1}{2}[1 \pm \cos(-\frac{\gamma J_1}{(h/m_n)\lambda^{-1}} + \frac{\gamma J_2}{(h/m_n)\lambda^{-1} + \lambda\omega/2\pi})]S(Q,\omega)w_\lambda(\lambda)\, d\omega\, d\lambda \tag{13}$$

After some more mathematics observing the distribution of incoming wavelengths and the distribution of deviations of the field integrals from their nominal value (inhomogeneity) the following approximate expression for the detected intensity is obtained:

$$I_{Det} \propto \frac{1}{2}\left[S(Q) \pm \frac{\exp(-\Psi^2)}{N} \cos(\delta\gamma \frac{m_n}{h}\lambda)\int \cos(J\lambda^3\gamma \frac{m_n^2}{2\pi h^2}\omega)\, S(Q,\omega)d\omega \right] \tag{14}$$

$\delta = J_1 - J_2$ is the asymmetry of the field integral between both spectrometer arms. Under the assumption that the incoming wavelength distribution and the distribution of field integrals around their nominal values are Gaussians, the following explicit relations hold: $N^2 = 1 + 4\Sigma^2\Lambda^2\gamma^2 m_n^2/h^2 \simeq 1$ and $\Psi^2 = [\Sigma^2\lambda_0^2 + \Lambda^2\delta^2]\gamma^2 m_n^2/h^2/N^2$. $\Sigma^2 = \langle \Delta J^2 \rangle /2$ relates to the field integral inhomogeniety and $\Lambda = \Delta_{FWHM}\lambda/4/\sqrt{\ln 2}$ to the full width at half maximum (FWHM) of the incoming wavelength distribution. For a given 10% wavelength width and $\lambda_0 = 1nm$ and $\Sigma = 2\times10^{-6}\mathrm{T}m$ the resulting resolution factor is $R = \exp(-\Psi^2) = 0.43$.

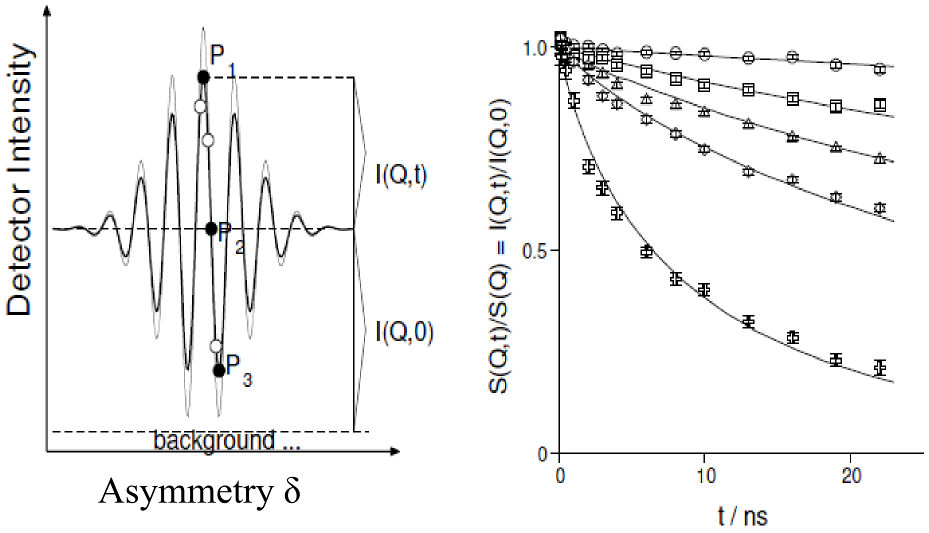

Fig. 3: *The left side indicates the detector intensity as obtained if the symmetry of the two precession fields is varied, the width of the echo oscillation group is inversely proportional to the width of the incoming wavelength (here as example more than 20% FWHM). The amplitude which may be determined by measuring 3 or more points and eventually by fitting the echo signal to the set of points ($\{P_1, P_2, \cdots, P_n\}$) compared to the maximum possible amplitude contains the spectroscopic signal which is obtained by NSE. The right side shows a typical set of results as obtained from a polymer melt with single chain contrast (i.e. a few protonated chains in a deuterated melt). Each point in that plot corresponds to one elementary amplitude determination. The various Fourier times result from different magnetic precession field settings and the various curves correspond to Q-values 0.05, 0.08, 0.12, 0.19 Å^{-1}. The lines are the predictions of the Rouse model[4,5,6].*

In an experiment , see Fig.3, the asymmetry δ is varied to determine the amplitude, A, of the first cosine factor in Eq.14:

$$A = \pm \underbrace{\exp(-\Psi^2)/N}_{=R} \int \cos(\underbrace{J\lambda^3\gamma\frac{m_n^2}{2\pi h^2}}_{=t}\ \omega)\ S(Q,\omega)d\omega \tag{15}$$

i.e. up to the resolution R the amplitude A is proportional to $S(Q,t)$. The resolution factor R is determined by measuring a reference sample with purely elastic scattering.

2.1 Example for Spin Echo Spectroscopy

The example presented here deals with the determination of the bending modulus of a microemulsion [7]. Microemulsions are thermodynamically stable mixtures of water and oil mediated by a surfactant. The typical structural sizes d of oil/water domains are in the order of d=20nm. Various structures can be obtained ranging from bicontinuous to lamellar microemulsions, depending on the interface properties and eventually their interaction. Different approaches have been developed for describing the physical properties of such microemulsions. Ginzburg-Landau models lead to a fair description of the scattering properties of a bicontinuous microemulsion [8,9].

$$S(Q) \propto \left(Q^4 - 2\left(Q_0^2 - \xi^{-2}\right)Q^2 + \left(Q_0^2 - \xi^{-2}\right)^2\right)^{-1} \tag{16}$$

with $Q_0 = 2\pi/d$ and ξ the correlation length. Eq.16 matches the scattering from the scattering length contrast between oil and water in the wave vector region between $Q < \delta Q_0$ ($\delta \approx 2\text{-}4$). On the other hand a description of the free energy in terms of interface bending contributions is commonly used, where the Helfrich free energy, F_{elastic}, is expressed as

$$F_{el} = \int dS \left[\frac{\kappa}{2}\left(c_1 + c_2 - 2c_0\right)^2 + \bar{\kappa} c_1 c_2 \right] \tag{17}$$

with $c_i = 1/R_i$ the local values of the principal curvature, c_0 the spontaneous curvature (here about zero) and $\kappa, \bar{\kappa}$ the bending modulus and the saddle splay modulus respectively. According to the Gauss-Bonnet theorem the latter term only contributes to the free energy changes when the surface topology changes.

By matching the Ginzburg-Landau free energy expression that underlies Eq.16 to a Gaussian random field approach, a relation between the parameters d and ξ of Eq.16 and the renormalized bending modulus κ entering Eq.17 can be established [10] :

$$Q_0 \xi = \frac{64}{5\sqrt{3}} \frac{\kappa_R}{k_B T} \Theta \tag{18}$$

where Θ approaches 1 for large enough κ. The elastic bending energy F_{el} of the surfactant membrane controls the phase behaviour. To get a deeper insight experimentally into the structure of microemulsions small angle neutron scattering (SANS) is used. The characteristic distance d and the correlation length ξ can be obtained from fitting Eq.16 to SANS data. Basically d determines the position of the maximum in the static structure factor S(Q), and ξ its width. Complementarily, the membrane fluctuation dynamics as investigated with neutron spin echo spectroscopy (NSE) also carries information on the interface bending modulus.

NSE allows the analysis of dynamic correlations in the neutron scattered intensity in the relevant SANS Q-regime.

Neutron spin echo spectroscopy measures the intermediate scattering function S(Q,t) usually given in the normalized form as relaxation function S(Q,t)/S(Q). In our example presented here, NSE data were taken in the so-called film contrast, i.e. deuterated oil and heavy water. Only the surfactant was protonated to assure proper contrast of the membrane only. The dynamics of fluctuating membranes in a microemulsion can be described by the model of a fluctuating membrane in a viscous medium, as has been proposed by Zilman und Grenek [11]. For small deformations of a nearly planar membrane, the free energy of deformation of an undulating patch of membrane can be described in terms of the Helfrich-Hamiltonian [12]:

$$H = \frac{1}{2}\kappa \int d^2 r \left[\nabla_{\vec{r}}^2 h(\vec{r}) \right]^2 = \frac{1}{2}\kappa \sum_{\vec{k}} k^4 h_{\vec{k}} h_{-\vec{k}} \tag{19}$$

where $h(\vec{r})$ denotes the amplitude of the undulation (the deviation of the membrane from a flat surface), and $h_{\vec{k}}$ its Fourier-components. The wave vector of the undulation modes is $\vec{k}$ and must not be confused with the scattering vector $\vec{Q}$. The Helfrich-Hamiltonian leads to the relaxation rate of $\left\langle h_{\vec{k}}(t) h_{-\vec{k}} \right\rangle_{Helfrich} = \left[k_B T / \left(\kappa k^4 \right) \right] \exp\left[-\omega(k) t \right]$ with $\omega(k) = \kappa k^3 / 4\eta$. Besides the bending modulus also the average viscosity η of the surrounding medium determines the characteristic times.

Assuming an ensemble of independent , randomly oriented membrane patches that obey the above relation, Zilman and Granek deduced an approximation for S(Q,t) in terms of a stretched exponential function, with a stretching exponent $\beta = 2/3$ [11].

$$S(Q,t) \simeq S(Q) \exp\left[-\left(\Gamma_Q t \right)^{\beta} \right] \quad with \quad \Gamma_Q = 0.025 \gamma_k \left(\frac{k_B T}{\kappa} \right)^{0.5} \frac{k_B T}{\eta} Q^3 \tag{20}$$

where $\gamma\kappa \approx 1-(3k_BT/4\pi\kappa) \ln (Q\xi) \rightarrow 1$ for $\kappa \gg k_BT$. The functional form of Eq.20 describes the NSE-relaxation data, see Fig.4, and the parameter β approaches 2/3 for large $Q > 4Q_0$ and $\Gamma_Q \sim Q^3$, however, the absolute value for κ inferred from Eq.20 is seemingly wrong. Further refinements of the Zilman-Granek model have to be considered in order to get a consistent picture of the NSE data with respect to SANS results. First of all, the variation of the structural length scale by changing the surfactant volume fraction changes the reduced relaxation rate $\Gamma^* = \left(\Gamma_Q / Q^3 \right) \eta(T) / k_B T$ significantly and next, the length scale of the structures considered that relates to the patch size of the model has to enter the final result. The full analysis of these refinements and to avoid further approximations that enter the Zilman-Granek model is shown in Ref. [7].

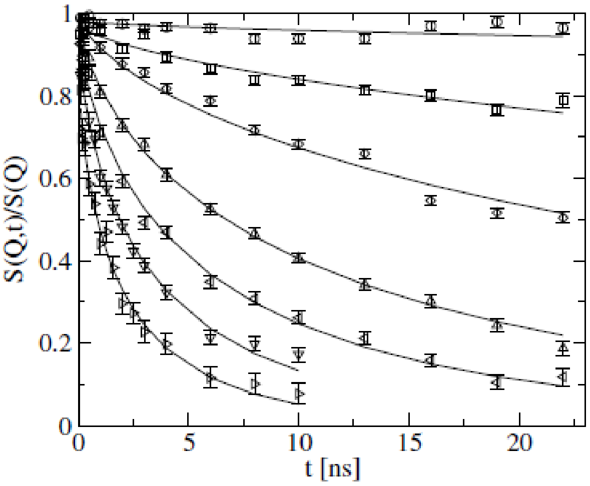

Fig. 4: *NSE spectra ($Q = 0.05 - 0.24Å^{-1}$) from a bicontinuous microemulsion fitted with a stretched exponential function where Γ_Q and β were separate fitting parameters for each curve. The β values approach 2/3 in the limit of high Q and $\Gamma_Q \sim Q^3$ [13].*

3 X-Ray Photon Correlation Spectroscopy

X-ray photon correlation spectroscopy, XPCS provides another method to measure the intermediate scattering function *S(Q,t)* on mesoscopic scales. Unlike NSE the accessed time domain for XPCS extends less towards the short time regime whereas correlation times of many seconds can be reached. XPCS is basically the same as photon correlation spectroscopy with visible light, also referred to as dynamic light scattering, DLS. It measures the intensity-intensity time auto-correlation function, g_2, of a speckle pattern in the scattered radiation, given by:

$$g_2\left(\vec{Q},t\right)=\left\langle I\left(\vec{Q},t_0\right)I\left(\vec{Q},t_0+t\right)\right\rangle/\left\langle I\left(\vec{Q},t_0\right)\right\rangle^2=1+A(Q)\left[S\left(\vec{Q},t\right)/S(\vec{Q})\right]^2 \tag{21}$$

where t is the correlation (delay) time. For an ergodic system, i.e. a fluid but not a glass or gel, < …. > denotes likewise a time or ensemble average. 0 < A(Q) < 1 is an optical contrast factor that depends on the experimental setup details. For the second equality the Siegert relation has been used to relate $\left[S\left(\vec{Q},t\right)/S\left(\vec{Q}\right)\right]^2$ to the intensity autocorrelation function. The principle of the instrumental setup is relatively simple as shown in Fig.5. The visibility of the time dependent correlation function depends on the coherence properties of the X-ray beam, and the size of the illuminated sample volume. The size of the effective sample region determines the size of the speckles, i.e. the solid angle ΔΩ, which an intensity peak or minimum covers in the random speckle texture of scattered intensity (see Fig.7). The detector element of area $\Delta x \Delta y$ must at most cover this solid angle, i. e. $\Delta\Omega \approx (\lambda/\Delta x)\ (\lambda/\Delta y)$. For example a sample of 30μm height (width) observed using a wavelength of λ=1.5Å and the detector at 5m distance allows for an opening height (width) of at most 25μm. If the detection area is enlarged the sample volume must be reduced. In other words a larger sample volume requires a smaller detection element. A way out of this intensity limiting trap is to use area detectors (CCD cameras) which have small-size individual pixels. However, these devices are not suited for online digital time correlation, but rather for time averaging as required to gain static information. Software correlation, on the other hand is limited to short times. There is clearly a need for fast solid-state detectors, like the Pilatus detector developed at the Paul-Scherrer Institute (PSI) in Switzerland. It has properties of a 2D detector, which allows for a reasonable number of pixel detection with each pixel calculating g_2 in real time with a time resolution of μs [14]. This offers new applications where an improved signal to noise ratio is required, such as the parallel variation of the Q-vector, the dynamics of crystallisation, to name just a few. Besides the detector pixel size, the ratio of source size and detector distance is another factor that enters the contrast A. The latter property is assigned to the beam as the transverse coherence length $\xi_{trans}=\xi_{x,y} = \lambda R/(2\pi\sigma_{x,y})$, which is to be compared to the sample size. The longitudinal coherence length of the beam is given by the degree of monochromatisation as $\Lambda_c = \lambda(\Delta E/E)/\pi$. For easily achievable monochromatisations of $\Delta E/E \approx 10^{-4}$, the effects of the transverse coherence lengths dominate up to $Q < 10^4\ 2\pi/\Delta x$. The required source characteristics, in combination with the necessary intensity are only provided by modern synchrotron radiation facilities. Indeed, from the mid nineties on such experiments were performed at all synchrotron machines of the third generation, where beam lines especially devoted for coherent experiments have been installed. In Europe these are the European Synchroton Radiation Facility (ESRF) in Grenoble/France, the Swiss Light Source (SLS) at PSI in Switzerland and in Hasylab at DESY in Germany.

In short, the coherence consideration boils down to the question on how the Q-resolution setup should be in order to resolve modulations of the size of the scattering volume (sample size).

The scattering contrast in the samples results from differences in the electron density which depend on the chemical structure. The very first successful experiments were therefore performed on colloidal metals [15]. However, as long as pure hydrocarbon particles without or with oxygen or nitrogen atoms included are considered, the scattering contrast is small and the intensities are correspondingly low. In these cases, area detection via a CCD camera is vital, but it limits the time resolution as discussed before. Using modern technologies with increased degree of coherence, beam-stability, number of (coherent) photons through the sample pinhole and higher energies etc., it is now possible to get to a sufficient signal-to-noise level even for soft matter samples, comparable to what is known from DLS.

Fig.5 shows the schematic layout of a XPCS beam line. A very thorough and up-to-date description of the method and very recent applications can be found in the review article by G. Grübel et al. in Ref.[16] and also at in the web-sites of the cSAXS beam line at the SLS in PSI in Switzerland and the Troika beam line ID10A at the ESRF in Grenoble in France [17].

XPCS is a new technique. Some inspection of recent publications shows how rapidly the field of application is growing. The topics span from biological imaging by hard X-ray diffraction microscopy [18], to the follow-up of atomic diffusion in $Cu_{90}Au_{10}$ by coherent X-rays [19], the dynamics of lamellar phases studied by XPCS and dynamic light scattering [20], to the problem on how the elastic behaviour of a viscoelastic liquid can be investigated using grazing incidence XPCS [21]. Regarding the physics of colloidal systems, aging and slow dynamics have been investigated [22]. Last but not least the dynamics of charged colloidal particles has been studied [23].

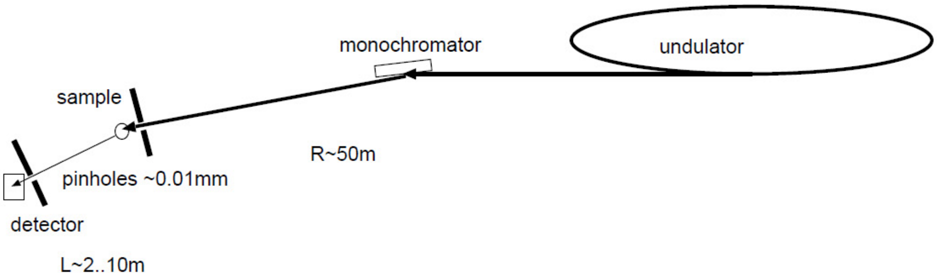

Fig. 5: *Schematic setup of a XPCS beam line at a synchrotron source. The effective X-ray source size is several 0.1mm. Besides a monochromator (e.g. a Si-single crystal), the instrument basically consists of a small pinhole in front of the sample defining the effective scattering volume plus a so-called guard slit which limits the primary beam so that only the small scattered intensity can be observed at the detector position. For a detailed discussion about the guard slit, see Fig.18-8 in Ref.16. A small pinhole in front of the detector limits the intensity collection to the solid angle to approximately the size of a typical speckle. For multispeckle detection with a CCD camera, the effective pinhole size is the size of one CCD pixel.*

It should be noted that the setup of a XPCS experiment is at the same time also an extremely good X-ray small-angle scattering machine. The regular SAXS spectrometers at synchrotron facilities are usually optimized for flux in order to achieve a sufficient short-time resolution for real-time experiments, for example for kinetic investigations or stopped flow experiments. At XPCS beam lines, the spatial resolution is unmatched since the contributions to the resolution, $\Delta Q/Q$, resulting from the finite slit width can be neglected. A typical example for the resolution capability is shown in Fig.8.

Another important issue is the radiation damage in polymeric, colloidal or biological samples caused by the X-rays. The local radiation dose applied to a small sample volume amounts to about 5-10kGy/s, for currently used beam lines (compared to less than 10^{-4} Gy/s for a typical neutron scattering experiment). In some cases, irradiation may be used to find interesting physics, as was observed for a charge-stabilized suspension of silica spheres in DMF with a concentration of about 160mg/g and in addition 20µM LiCl. This system shows a crystalline FCC six-fold symmetric structure, in agreement with the theoretical phase diagram prediction at the given number densities of particles and the salt concentration. This is shown in the upper left picture of Fig.6, where Bragg peaks are observed in the small-angle scattering configuration. Pictures were taken for 0.1s exposure time while the X-ray beam was on. After 1000s of exposure structure has melted (see the picture in upper right corner).

The structure recovers after the beam has been switched off, (see lower row in Fig.6) reaching the starting condition again after 2000s. Obviously, the X-ray beam has created screened type of charges within the sample, which lead to melting, in plausible agreement with theoretical calculations. Switching-off the beam leads to the recovery of the structure, since previously formed charges and/or radicals do recombine.

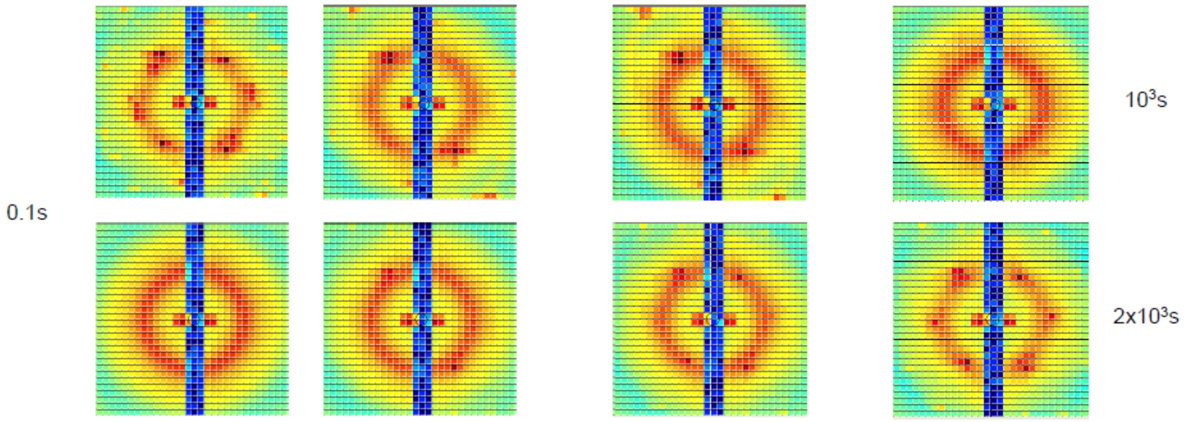

Fig. 6: *Structure melting and recovery from a Si/DMF colloidal suspension with 20µM LiCl added, under the influence of x-ray beam from cSAXS at SLS. The upper row shows melting occurring after 1000s, whereas the lower row shows recovery of the structure 2000s after the beam has been interrupted. Each picture was taken for the duration of 0.1s.*

3.1 Examples for X-ray Speckle Pattern

A speckle pattern was first investigated by Sutton and Mochrie et al. in their pioneering paper from 1991 [24] showing a Frauenhof-Diffraction pattern from a crystal, which clearly demonstrated the sufficient degree of coherence of the synchrotron X-ray beam. The authors predicted at the time of their discovery that dynamic experiments would become feasible.

As an example for a static scattering pattern, the X-ray speckle pattern from a porous silica glass is shown in Fig.7:

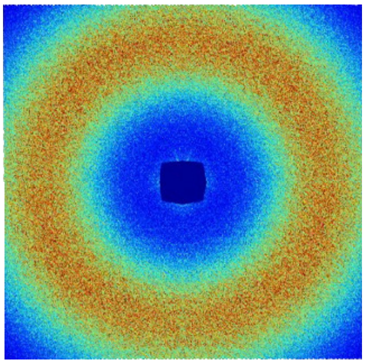

Fig. 7: *Static speckle pattern from a porous silica glass.*

The scattering of coherent light from a disordered system gives rise to a random diffraction or speckle pattern, long known from laser light scattering. The speckles are related to the exact spatial arrangement of the disorder. Such information is not accessible with incoherent light because the diffraction pattern observed in an ordinary diffraction experiment is typically an ensemble average containing only information on the average correlations in the sample. If the spatial arrangement changes with time, the corresponding speckle pattern also changes. The intensity fluctuations of the speckles thus provide information about the underlying dynamics (see section3.2.).

Consider again Fig.7. With a coherent beam of cross section ξ^2_{trans}, incident wave vector $\vec{k}$ and scattered wave vector $\vec{k}'$ scattered from a disordered sample. The instantaneous intensity I at a given point in the far field can be written as the square of a total field $\vec{E}(\vec{Q},t)$ according to

$$I(\vec{Q},t) = \left|\vec{E}(\vec{Q},t)\right|^2 = \left|\sum_n b_n(\vec{Q}) \exp\left[iQ \cdot \vec{r}_n(t)\right]\right|^2 \tag{22}$$

Here, $b_n(\vec{Q})$ is the scattering amplitude of the n-th scatterer located at position $\vec{r}_n$(t) at time t, and $\vec{Q} = \vec{k} - \vec{k}'$ in units of ħ. is the momentum transfer. The sum is taken over scatterers in the coherence volume, spanned by the transverse and longitudinal coherence lengths. The field in Eq.22 may be also expressed in terms of electron density function, ρ ($\vec{r}'$), as

$$\vec{E}(\vec{Q},t) = \int d\vec{r}'\, \rho(\vec{r}') \exp\left[i\vec{Q} \cdot \vec{r}'(t)\right] \tag{23}$$

A measurement of the intensity will naturally invoke a time average $< I(\vec{Q},t) >_T$ over the acquisition time T, but it does not involve any statistical ensemble average. If the system is not ergodic, i.e. has random static disorder, $< I(\vec{Q},t) >_T$ will display as a function of $\vec{Q}$ distinct and sharp variations in intensity, known as speckles. If, on the other hand, the system behaves ergodic, with fluctuations on time scales very short compared to the counting time, the measured time average is equivalent to an ensemble average, and $< I(\vec{Q},t) >_T$ can be replaced by the usual ensemble average denoted by $< I(\vec{Q},t) >$ The observed scattering is then featureless, apart from time averaged correlations in the sample similar to a regular scattering experiment with incoherent radiation. In Fig.7, a static speckle pattern from a porous silica glass is shown. The observed ring structure with a maximum in the intensity at $Q(I_{\max})$ is due to pore-pore correlations in the glass. Static X-ray speckles have been observed in a large variety of different systems, i.e. porous systems [25], modulated bulk and surface structures [26], magnetic materials [27] and in systems exhibiting domain disorder [24].

3.2 Example for XPCS Dynamics

Long-time dynamics of charge-stabilized colloids: is there dynamic scaling or not?

Charge-stabilized suspensions are ubiquitously found in chemical and waste-treatment industries, and in medical and biological products. These systems are composed of meso-scaled colloidal particles dispersed in a low-molecular polar solvent like water. Examples include proteins and viruses, paint and clay particles, and well-characterized model systems consisting of spherical charge-stabilized particles. The beauty of the XPCS method is mainly due to the fact that different to dynamic light scattering, the sample can be completely opaque and may consist of particles with sizes in the order of the inverse Q-range accessible by the method. The study discussed now [28], takes advantage of this fact and deals with the question, on whether the dynamic scaling behaviour of the dynamic structure factor, observed experimentally for hard spheres in the work by Segrè and Pusey [29], holds true also for charge-stabilized particles. According to Segrè and Pusey, the decay of the dynamic structure factor of PMMA spheres for values Qd > 2.5, where d is the hard-sphere diameter, is controlled by self-diffusion according to:

$$S(Q,t)/S(Q) = \exp\left(-Q^2 W(t) \times D_s(Q)/D_s\right) \tag{24}$$

Here, W(t) is the particle mean-squared displacement (divided by 6) of short-time slope D_S, and $D_S(Q)$ characterizes the short-time exponential decay of S(Q,t). At long times, this factorization of the wave number and time dependence of S(Q,t) leads to a single-exponential decay, $S(Q,t)/S(Q) = \exp(-Q^2 D_L(Q)\, t)$, with a long-time diffusion function given by $D_L(Q) = D_S(Q) \times D_L/D_S$, where D_L is the long-time self-diffusion coefficient. It is especially interesting to perform XPCS experiments at a wave number $Q_s > Q_m$ where $S(Q_s) = 1$, and to check whether an estimate for the (long-time) self-diffusion coefficient can be obtained from this measurement as suggested by Pusey [30]. Note here that this kind of measurement could not been performed for this present system with dynamic light scattering, mainly for the reason that S(Q) can not be accessed within the Q-range of light scattering.

We have systematically explored the short-time and long-time dynamics of strongly interacting charged-stabilized particles in the fluid regime up to the liquid-crystal phase transition. The studied system consists of silica spheres of 164 nm diameter dispersed in dimethyl-formamide (DMF).

The X-ray synchrotron beam at energy of 8.7 keV from the cSAXS beam line at the SLS in PSI/Swiss was carefully collimated to reach high brilliance while keeping sufficient transversal coherence, a crucial requirement in the XPCS experiment. The sample was initially characterized by measuring the scattered intensity using the 2D Pilatus detector. Numerous visible minima in the high scattering vector *Q*-range provide a proof that the sample is very mono-disperse.

In further studies the point detector was used to measure the low-Q part of I(Q) required for calculation of the colloidal suspension structure factor *S*(Q). At selected Q-values, the time auto-correlation function was measured by means of a digital auto-correlator, see Fig.9. It should be stressed that the quality of the correlation functions (in terms of the contrast and the noise) measured here by using XPCS correlation spectroscopy are comparable to those from using visible light.

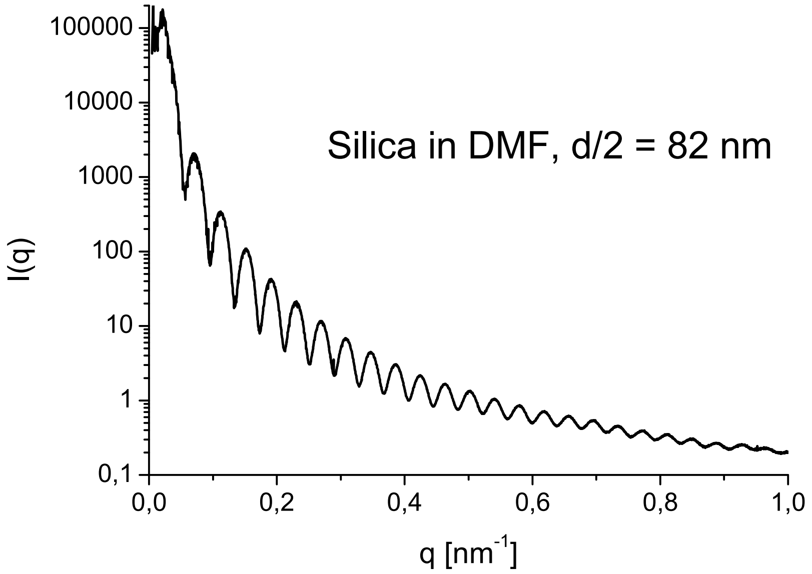

Fig. 8: *Pronounced multiple minima in the scattered intensity pattern prove that the sample is extremely mono-disperse.*

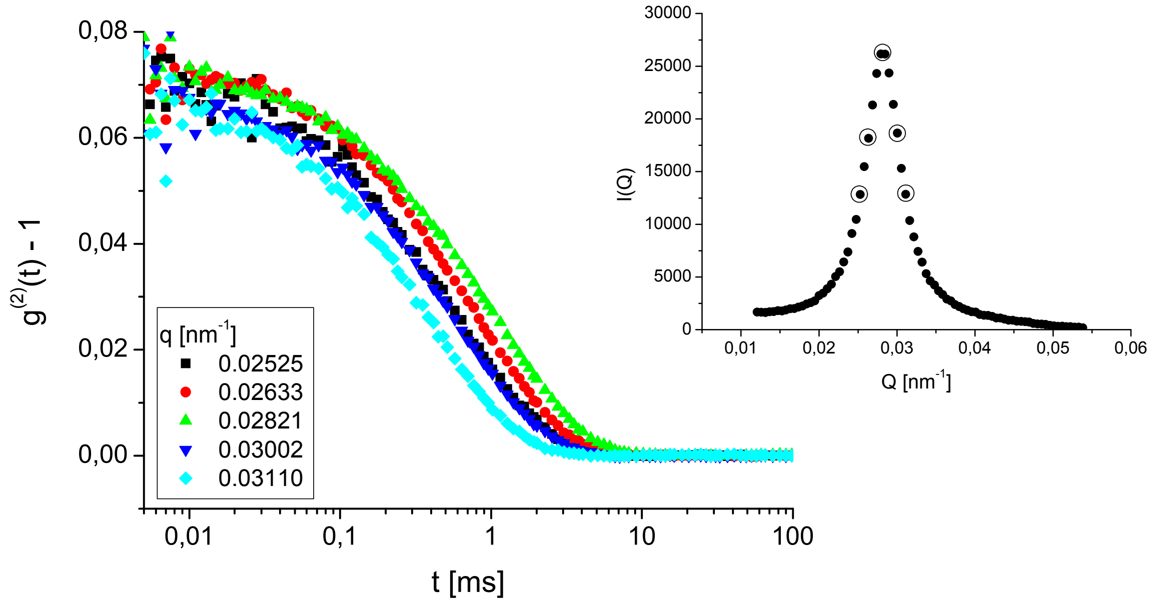

Fig. 9: *Intensity auto-correlation functions at Q-values as indicated. The circles in the inset are X-ray data for I(Q).*

Each correlation function was analyzed in terms of the initial decay of ln $g(t)$, as shown in Fig.10. The slope of ln $g_2(t)$ relates to $D(Q)Q^2$, where $D(Q)$ is the collective diffusion coefficient. From the initial decay part the short-time diffusion coefficient, $D_s(Q)$, was calculated, while from the slope of the long-time part, the long-time collective diffusion coefficient, $D_l(Q)$ was estimated, cf. Fig.10. The results of the fits are presented in Fig.11. Following the scaling idea of Segre, Pusey and others [29], we have scaled the correlation functions according to the formula

$$f(Q,t) = \frac{\ln g^{(1)}(t)}{D_s(Q)\,Q^2} \tag{25}$$

In accordance with the scaling prediction, all functions measured at Q values not smaller than the peak position value follow a single master curve.

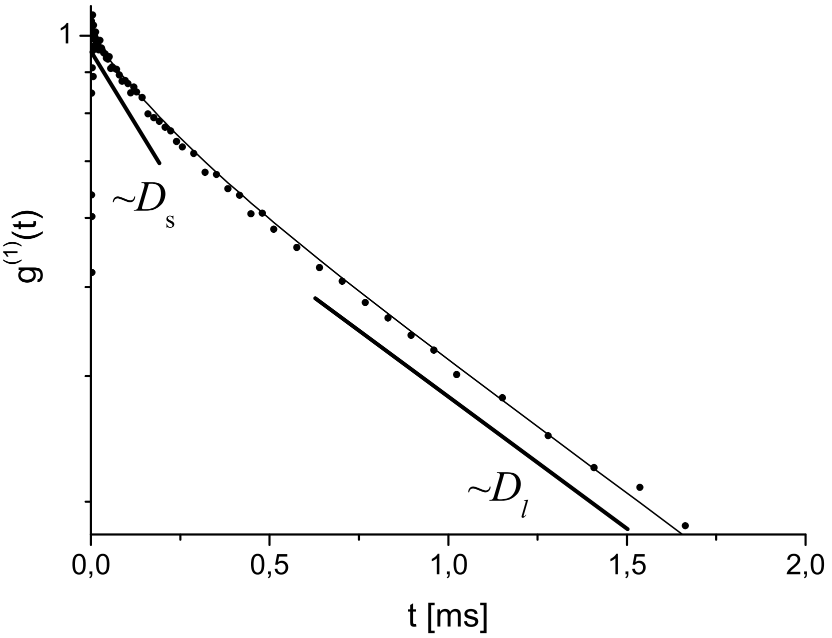

Fig. 10: *The initial decay of ln g(t). The thick lines indicate the slopes of the initial (short-time) and final (long-time) decay of ln g(t).*

We can conclude from our experimental findings that thanks to the extremely efficient XPCS setup at PSI, it has been possible to obtain high-quality time-correlation functions of a charged colloidal system. In our study, we have used a highly mono-disperse and strongly interacting system of silica spheres in DMF. The measurements of XPCS correlation functions for a series of chosen Q-values around the main structure peak position Q_m, yielded short- and long-time diffusion coefficients derived from the decay of ln $g(t)$. Scaling of ln $g(t)$

with $D_s(Q)\ Q^2$ allowed for creating a master curve onto which all functions measured at Q-values not smaller than Q_m, collapse in agreement with the scaling prediction., cf. Figs.12a,b. The present XPCS result for the dynamic scaling behavior of the S(Q,t) for Silica in DMF nicely confirms corresponding DLS findings for a different system by Holmqvist and Nägele [31].

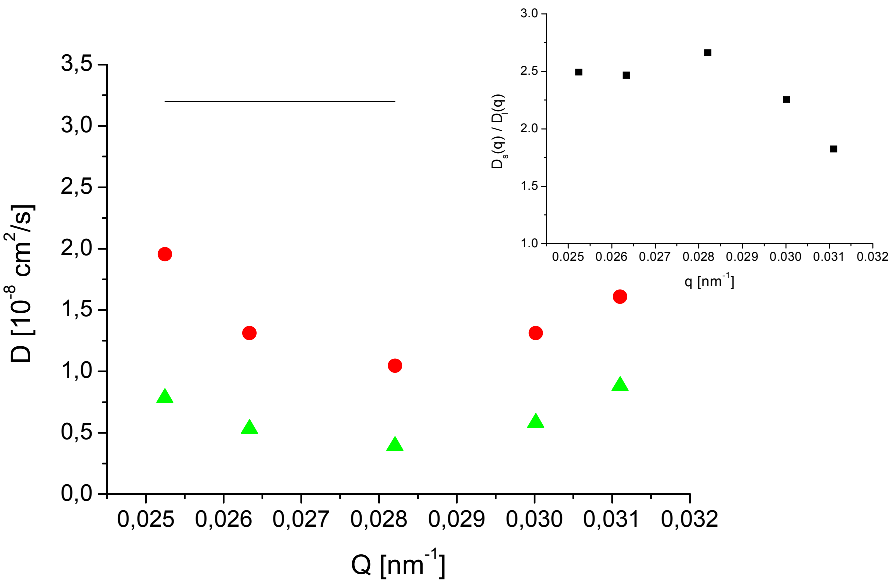

Fig. 11: *Values of short-time ($D_s(Q)$)(●) and long-time ($D_l(Q)$) (▲) collective diffusion coefficients, obtained from the slopes of the initial and final decay of ln g(t). (—) denotes the value for D_0. The inset shows the ratio of $D_l(Q)$ / $D_s(Q)$.*

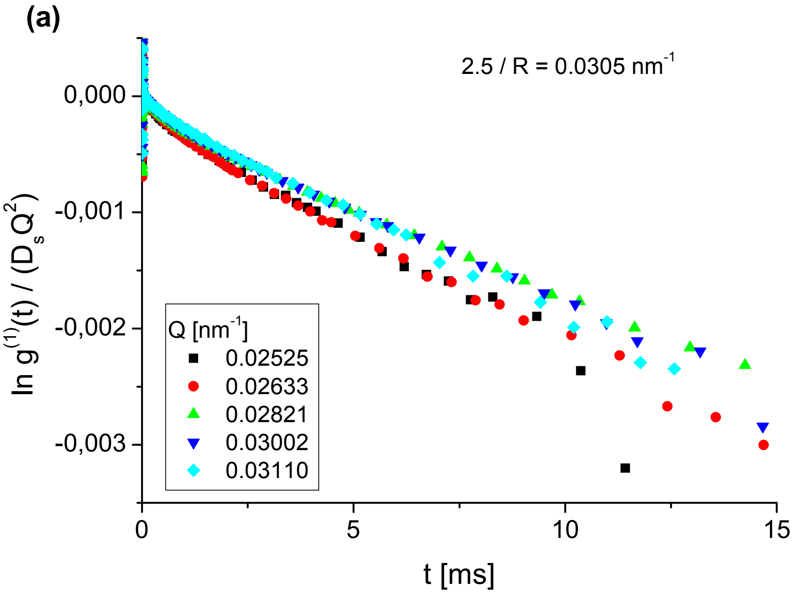

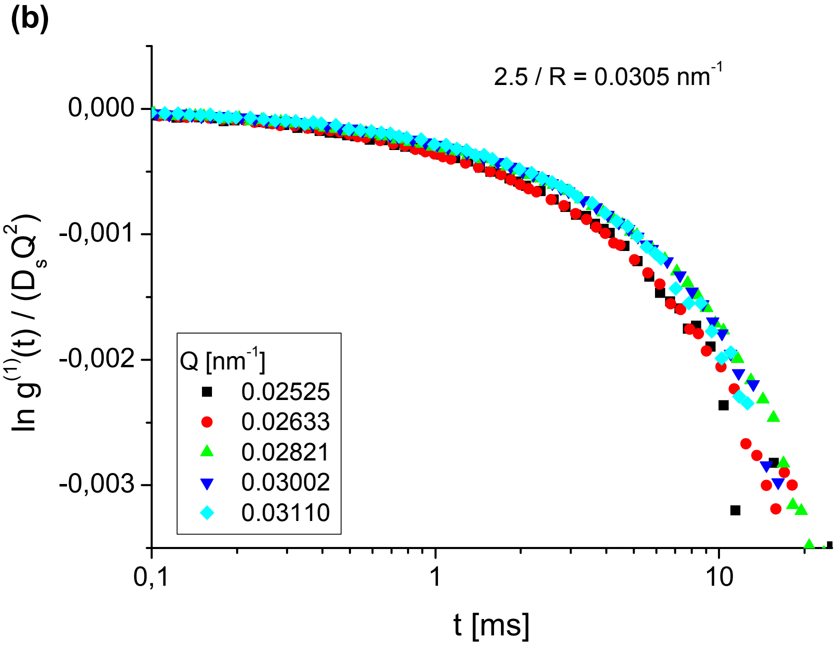

Fig. 12: *Scaled correlations functions measured at the Q-values of the peak of S(Q) and at Q-values lying symmetrically on both sides of the peak (cf. inset of Fig.9).*

References

[1] F. Mezei (ed.), Neutron Spin Echo, Lecture Notes in Physics, Vol. 128, Springer (1980)

[2] F. Mezei, C. Pappas and T. Gutberlet (eds.) Neutron Spin Echo Spectroscopy, Lecture Notes in Physics, Vol.601, Springer (2003)

[3] M. Monkenbusch, R. Schätzler and D. Richter, Nuclear Instruments & Methods In Physics Research Section A- Accelerators Spectrometers detectors And Associated Equipment **399**, 301 (1997)

[4] P. Rouse; J. Chem. Phys., **21**, 1250 (1953)

[5] M. Doi and S. Edwards, The Theory of Polymer Dynamics, Oxford University Press. Oxford (1994)

[6] M. Monkenbusch, IFF-springschool 2006, chapter D6

[7] M. Monkenbusch, O. Holderer, H. Frielinghaus, D. Byelov. J. Allgaier and D. Richter, J. Phys.: Condens. Matter **17**, 2903 (2005)

[8] G. Gompper and G. Schick in: *Phase Transitions and Critical Phenomena.* C. Domb and J. Lebowitz (eds.) Academic Press London (1994)

[9] M. Teubner and R. Strey, J. Chem. Phys. **87**, 3195 (1987)

[10] H. Endo, M. Mihailescu, M. Monkenbusch, J. Allgaier, D. Richter, B. Jakobs, T. Sottmann, R. Strey and I. Grillo, J. Chem. Phys. **115**, 580 (2001)

[11] A. Zilman and R. Granek, Phys. Rev. Lett. **77**, 4788 (1996)

[12] W. Helfrich, Z. Naturf. **28**, 693 (1973)

[13] O. Holderer, H. Frielinghaus, D. Byelov, M. Monkenbusch, J. Allgaier and D. Richter, J Chem. Phys. **122**, 094908 (2005)

[14] http://pilatus.web.psi.ch/pilatus.htm

[15] T. Thurn-Albrecht, W. Steffen, A. Patkowski, G. Meier, E. W. Fischer, G. Grübel and D. Abernathy, Phys. Rev. Lett. **77**, 5437 (1996)

[16] G. Grübel, A. Madsen and A. Robert in: *Soft Matter Characterisation.* R. Borsali and B. Pecora (eds.) Springer (2008) chapter 18, pages 954-995

[17] http://www.esrf.eu/UsersAndScience/Experiments/SoftMatter/ID10A/; http://www.psi.ch/sls/csaxs/csaxs

[18] E. Lima, L. Wiegart, P. Pernot, M. Howell, J. Timmins, F. Zontone and A. Madsen; Phys. Rev. Lett. **103**, 198102 (2009)

[19] M. Leitner, B. Sepiol, L.-M. Stadler, B. Pfau and G. Vogl, Nature Mat. **8**, 717 (2009)

[20] D. Constantin, G. Brotons, T. Salditt, É. Freyssingeas and A. Madsen, Phys Rev E **74**, 031706 (2006)

[21] Y. Chushkin, C. Caronna and A. Madsen, Europhys. Lett. **83**, 36001 (2008)

[22] A. Fluerasu, A. Moussaïd, A. Madsen and A. Schofield, Phys Rev.E **76**, 010401 (2007)

[23] A. Banchio, J. Gapinski, A. Patkowski, W. Häussler, A. Fluerasu, S. Sacanna, P. Holmqvist, G. Meier, M. P. Lettinga and G. Nägele, Phys. Rev. Lett. **96**, 138303 (2006)

[24] M. Sutton, S. G. J. Mochrie, T. Greytak, S. E. Nagler, L. E. Berman, G. A. Held and G. B. Stephenson, Nature **352**, 608 (1991)

[25] D. L. Abernathy, G. Grübel, S. Brauer, I. McNulty, G. B. Stephenson, S. G. J. Mochrie, A. R. Sandy, N. Mulders and M. Sutton, J. Synch. Rad. **5**, 37 (1998)

[26] Z. H. Cai, B. Lai, W. B. Yun, I. McNulty, K. G. Huang and T. P. Russel, Phys. Rev. Lett. **73**, 82 (1994)

[27] F. Yakhou, A. Letoublon, F. Livet, M. de Boissieu and F. Bley, J. Magn. Magn. Mater. **233**, 119 (2001)

[28] J. Gapinski, A. Patkowski and G. Meier, personal communication

[29] P.N. Segrè and P.N. Pusey, Phys. Rev. Lett. **77**, 771 (1996)

[30] P.N. Pusey, J. Phys. A: Math. Gen. **11**, 119 (1978)

[31] P. Holmqvist and G. Nägele, Phys. Rev. Lett. **104**, 058301 (2010)